

---

# HYBRID FULL-FIELD THERMAL CHARACTERIZATION OF ADDITIVE MANUFACTURING PROCESSES USING PHYSICS-INFORMED NEURAL NETWORKS WITH DATA

---

Shuheng Liao, Tianju Xue, Jihoon Jeong, Samantha Webster, Kornel Ehmann, Jian Cao

Department of Mechanical Engineering  
Northwestern University  
Evanston, IL, 60208, USA

## ABSTRACT

Understanding the thermal behavior of additive manufacturing (AM) processes is crucial for enhancing the quality control and enabling customized process design. Most purely physics-based computational models suffer from intensive computational costs, thus not suitable for online control and iterative design application. Data-driven models taking advantage of the latest developed computational tools can serve as a more efficient surrogate, but they are usually trained over a large amount of simulation data and often fail to effectively use small but high-quality experimental data. In this work, we developed a hybrid physics-based data-driven thermal modeling approach of AM processes using physics-informed neural networks. Specifically, partially observed temperature data measured from an infrared camera is combined with the physics laws to predict full-field temperature history and to discover unknown material and process parameters. In the numerical and experimental examples, the effectiveness of adding auxiliary training data and using the technique of transfer learning on training efficiency and prediction accuracy, as well as the ability to identify unknown parameters with partially observed data, are demonstrated. The results show that the hybrid thermal model can effectively identify unknown parameters and capture the full-field temperature accurately, and thus it has the potential to be used in iterative process design and real-time process control of AM.

**Keywords** Machine learning · Data-driven model · Inverse problem · Directed energy deposition · Heat transfer

## 1 Introduction

Metal additive manufacturing (AM) processes have been increasingly utilized in various industries like aerospace, automotive, and biomedical industries because of their high flexibility in fabricating complex geometries with various materials. Directed energy deposition (DED) and Powder bed fusion (PBF), are the two major types of metal additive manufacturing processes. In both DED and PBF, a high energy laser moves along a pre-defined toolpath and melts the material to build the part in a layer-by-layer manner. Understanding the highly transient thermal behavior of AM processes can help to maintain the process stability and part quality because it is strongly related to the process defects such as lack of fusion, porosity, and cracking. In addition, thermal history is also a key link in the process-structure-property chain of the material in AM processes [Smith et al., 2016]. Therefore, developing efficient and reliable thermal models of AM processes is crucial for enhancing the process quality control as well as for process design.

Physics-based computational models using finite element method (FEM) and computational fluid dynamics (CFD) have been widely studied to predict thermal behavior in AM processes. Thermal-fluid models [Mukherjee et al., 2018a,b], considering the heat transfer in the entire part and fluid flow within the melt pool by solving the Navier-Stokes equations including energy conservation, are considered as high-fidelity computational models for predicting the thermal behavior. Gan et al. [Gan et al., 2017] improved the thermal-fluid model by considering heat loss due to vaporization. It was shown through the NIST AM benchmark exercise [Gan et al., 2019, Heigel et al., 2020] that the model with vaporization reduced the average difference between the numerical and experimental cooling rates during solidification from 28% to 12% compared to that without fluid flow and vaporization. However, the difference in the

---

cooling rate after solidification does not vary too much. In most cases, the CFD models are computationally expensive and are usually performed at mesoscale. FEM models [Roberts et al., 2009, Gao et al., 2016], considering only the solid heat transfer in AM processes, are computationally less expensive than CFD models and thus can be applied to the simulation of macroscopic distortion [Denlinger and Michaleris, 2016] and residual stress [Lu et al., 2019, Li et al., 2022], as well as offline process design and planning [Liao et al., 2022, Irwin et al., 2021]. However, these FEM models are still too time-consuming for time-sensitive applications like online process control. In addition, using conventional physics-based models requires accurate input of material and process parameters, which is usually costly to obtain from experiments, to avoid significant discrepancies between the model and actual experimental conditions.

In the past few years, data-driven prediction models in advanced manufacturing have gained increasing attention because of their potential to derive end-to-end models directly from big data and improve computational efficiency with the latest computational tools based on graphic process units (GPUs). In our early work [Mozaffar et al., 2018], a data-driven model based on recurrent neural networks (RNNs) was developed to predict the thermal history from the time-series toolpath features, geometric features and laser features, and the results showed that the model reaches less than  $3e-5$  normalized mean squared error (MSE) after the training of 100 epochs with the dataset generated from FEM simulations. More recently, Roy et al. [Roy and Wodo, 2020] developed a machine learning model of thermal history in AM. In their model, the G-code is directly translated into a set of input features, e.g., distance from heat source and cooling surface, for predicting the local thermal history. The model was trained with FEM simulation data and the prediction error was less than 5% in almost real time. Ren et al. [Ren et al., 2020] developed a data-driven model predicting the thermal field evolution of a single layer built from different toolpath strategies in AM, where 100 different one-layer deposition cases with 6 different toolpath strategies were simulated using FEM for generating the dataset and the model achieved a prediction accuracy of 95% after the training. Zhou et al. [Zhou et al., 2021] extended the idea and developed the thermal field prediction model for arbitrary multi-layer geometries by proposing a novel method for the discretization of the deposition process, and achieved an accuracy exceeding 94% in the validation dataset. In our recent work [Mozaffar et al., 2021], a geometry-agnostic thermal model based on graph neural networks (GNNs) was proposed where the FEM simulation data was converted into a graph representation to train the GNN model. With the dataset generated from 50 different geometries, the trained model can predict the thermal history for unseen geometries with a root-mean-square error (RMSE) less than  $1e-2$ . Although data-driven models have been demonstrated to be computationally efficient, these models require a large amount of labeled training data, which is often impractical to be obtained from the experiment. Most of the studies listed above, and other previous studies [Stathatos and Vosniakos, 2019, Ness et al., 2022] used FEM simulation to generate the training dataset, in which case although the prediction accuracy is good compared with the simulation data, the models are still not directly connected with the actual experimental conditions and the accuracy strongly relies on the fidelity of the simulation models.

In this work, we propose a hybrid (both physics-based and data-driven) framework that allows to arbitrarily fuse “big data” (simulations) and/or “small data” (experiments) into a physics-informed model, hence providing a customized, flexible platform for efficient thermal analysis in AM. Our approach is based on physics-informed neural networks (PINNs), originally proposed by Raissi et al. [Raissi et al., 2019] as a surrogate model to solve partial differential equations (PDEs). PINNs have been widely used to solve forward problems, i.e., solving PDEs, and inverse problems, i.e., identifying parameters, in engineering applications like fluid mechanics [Raissi et al., 2020, Mao et al., 2020], heat transfer [Cai et al., 2021, Laubscher, 2021], and solid mechanics [Haghighat et al., 2021, Zhang et al., 2020]. PINNs provide a way to define the loss function from the governing equations. By combining the PINN model with the labeled data, a hybrid model can be developed which takes advantage of physics laws to eliminate the need for large training datasets, and in return, allowing the discovery of unknown physics from the data. In a recent work by Zhu et al. [Zhu et al., 2021], PINNs were applied to predict the thermal field in AM, where the physics parameters were assumed to be known, and the FEM simulation data was used to train the PINN model. Here, we developed a hybrid framework for AM processes using PINNs for the first time, where partially observed temperature data measured from an infrared (IR) camera is combined with the physics laws to predict the full-field temperature history. We also demonstrate that it can be further used to discover unknown material and process parameters.

The rest of the paper is organized as follows. In Section 2, the governing equation of the heat transfer problem and the basic formation of PINNs are introduced. In Section 3, a numerical example of bare plate scanning is performed where the effect of auxiliary data and transfer learning in solving forward problems are studied, and the ability of identifying unknown parameters from partially observed data is demonstrated. In Section 4, an experimental case of a DED thin wall part, where PINN is used to predict the full-field temperature data is presented. Conclusions and future work are given in Section 5.

## 2 Methods

Figure 1 illustrates the proposed hybrid framework. The neural network takes the spatial-temporal coordinates as the input and predicts the temperature at the corresponding point. The loss function is defined as the combination of the residuals of the PDEs, the boundary conditions (BCs) and the initial conditions (ICs), as well as an extra data-based loss term where the experimental temperature data measured by an IR camera is used as the ground truth. In the following subsections the governing equations of the heat transfer problem in AM and the basic formation of PINNs are introduced.

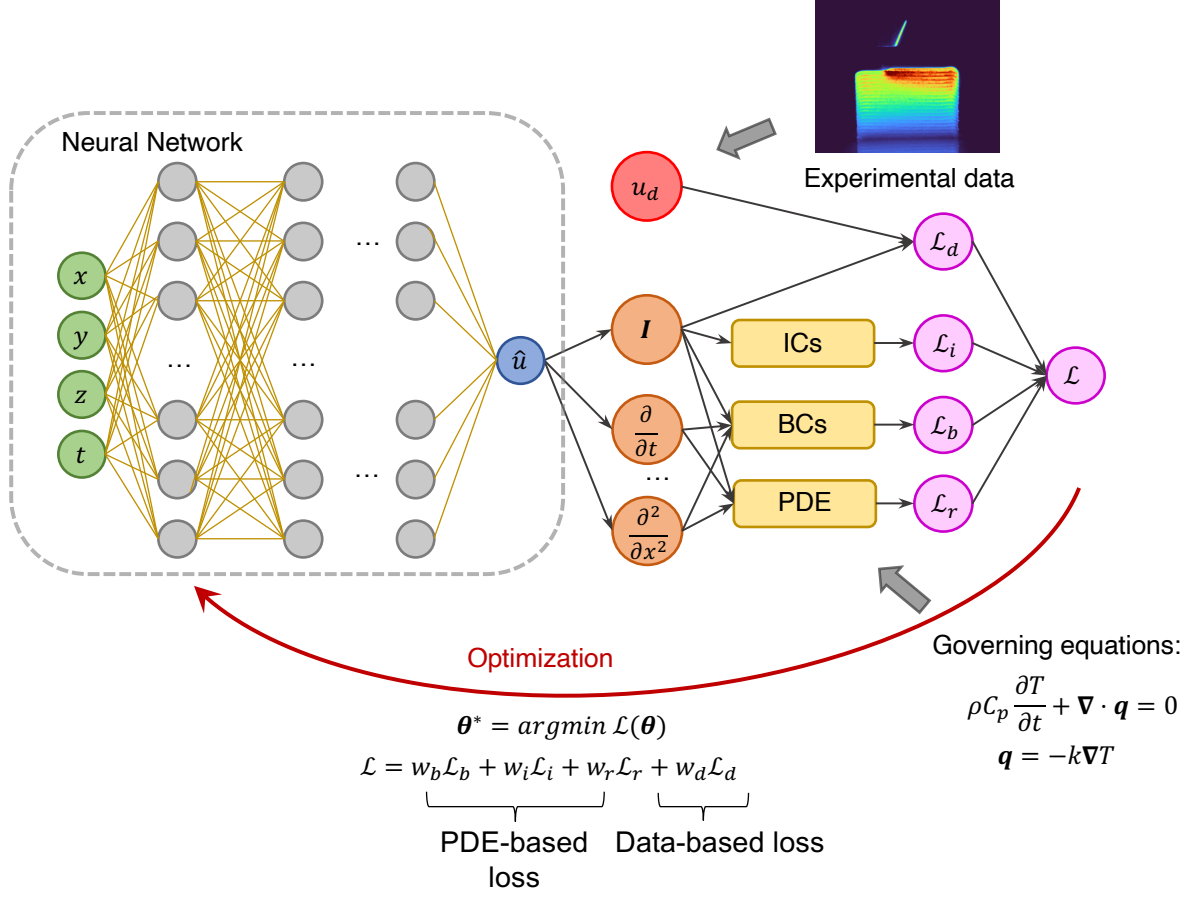


Figure 1: Hybrid thermal modeling framework for AM based on PINNs.

### 2.1 Governing equations

In this work, to demonstrate the hybrid framework, we model the heat conduction in AM, while fluid flow and vaporization heat loss are ignored. It is noted that adding the implementation of these additional physics in the framework will be relatively easy since PINN is a meshless optimization-based approach compared to the conventional finite element or finite difference method. The governing equation of the transient heat conduction in AM can be written as:

$$\rho C_p \frac{\partial T}{\partial t} + \nabla \cdot \mathbf{q} = 0, \quad (1)$$

where  $\rho$  is the density of the material,  $C_p$  is the heat capacity,  $T$  is temperature,  $t$  is time and  $\mathbf{q}$  is the heat flux, which is given by the Fourier's Law:

$$\mathbf{q} = -k \nabla T, \quad (2)$$

where  $k$  is the thermal conductivity of the material. The heat flux boundary condition in AM processes can be described as:

$$\mathbf{q} \cdot \mathbf{n} = q_{\text{laser}} + q_{\text{conv}} + q_{\text{rad}}, \quad (3)$$

where  $q_{\text{laser}}$ ,  $q_{\text{conv}}$ , and  $q_{\text{rad}}$  are the heat flux due to the laser heat source, convection and radiation, respectively. The laser heat flux is modeled using a Gaussian surface heat flux model:

$$q_{\text{laser}} = -\frac{2\eta P}{\pi r_{\text{beam}}^2} \exp\left(\frac{-2d^2}{r_{\text{beam}}^2}\right), \quad (4)$$

where  $\eta$  is the laser absorptivity,  $P$  is the laser power,  $r_{\text{beam}}$  is the laser beam radius, and  $d$  is the distance from the material point to the laser center. The convective and radiative heat flux can be calculated by:

$$q_{\text{conv}} = h(T - T_0), \quad (5)$$

$$q_{\text{rad}} = \sigma\varepsilon(T^4 - T_0^4), \quad (6)$$

where  $h$  is the convection heat transfer coefficient,  $\sigma$  is the Stefan–Boltzmann constant,  $\varepsilon$  is the emissivity of the material and  $T_0$  is the ambient temperature. The laser heat flux is assumed to be applied on only the top surface while the convective and radiative heat flux are applied on all surfaces except for the bottom surface of the substrate, where a Dirichlet boundary condition is applied:

$$T|_{z=0} = T_0. \quad (7)$$

## 2.2 Physics-informed neural networks

PINNs are neural networks with physics information encoded. The basic idea of PINN is to approximate the solution of PDEs using a neural network, which is trained by minimizing a loss function defined based on the residuals of the PDEs, BCs, and ICs. Considering a PDE defined in the spatial-temporal domain of the general form:

$$u_t(\mathbf{x}, t) + \mathcal{N}[u] = 0, \quad \mathbf{x} \in \Omega, t \in [0, T], \quad (8)$$

where  $u(\mathbf{x}, t)$  is the solution of the PDE,  $\mathcal{N}[\cdot]$  is a general differential operator;  $\mathbf{x}$  and  $t$  are the spatial and temporal coordinates,  $\Omega$  is the computational domain which is a subset of  $\mathbb{R}^3$ . The BCs and ICs of the PDE can be written as:

$$\mathcal{B}(u, \mathbf{x}, t) = 0, \quad \mathbf{x} \in \partial\Omega, \quad (9)$$

$$u(\mathbf{x}, 0) - I(\mathbf{x}) = 0, \quad \mathbf{x} \in \Omega, \quad (10)$$

where  $\partial\Omega$  is the boundary of the computation domain. In the framework of PINN,  $u$  is approximated using a fully connected neural network, of which the input is  $\mathbf{x}$  and  $t$ , and the output is the approximated solution  $\hat{u}(\mathbf{x}, t)$ . The loss function of PINN is defined as:

$$\mathcal{L} = w_b \mathcal{L}_b + w_i \mathcal{L}_i + w_r \mathcal{L}_r, \quad (11)$$

where  $\mathcal{L}_b$ ,  $\mathcal{L}_i$ , and  $\mathcal{L}_r$  are the losses from BCs, ICs and the PDE residuals, respectively, and  $w_b$ ,  $w_i$  and  $w_r$  are the weights of each term. When training a PINN, sampling points are first selected at the boundary, at the initial state, and in the temporal-spatial domain. At each iteration, each loss term can be calculated at its respective sampling points:

$$\mathcal{L}_b = \frac{1}{N_b} \sum_{k=1}^{N_b} |\mathcal{B}(\hat{u}(\mathbf{x}_b^k, t_b^k), \mathbf{x}_b^k, t_b^k)|^2, \quad (12)$$

$$\mathcal{L}_i = \frac{1}{N_i} \sum_{k=1}^{N_i} |\hat{u}(\mathbf{x}_i^k, 0) - I(\mathbf{x}_i^k, 0)|^2, \quad (13)$$

$$\mathcal{L}_r = \frac{1}{N_r} \sum_{k=1}^{N_r} |\hat{u}(\mathbf{x}_r^k, t_r^k) - \mathcal{N}[\hat{u}]|^2, \quad (14)$$

where  $N_b$ ,  $N_i$ , and  $N_r$  are the number of the sampling points for each loss term. PINNs use automatic differentiation (AD), a method commonly used in neural network applications [Baydin et al., 2018] and integrated with most of the deep learning packages like TensorFlow [Abadi et al., 2016] and PyTorch [Paszke et al., 2017], to automatically evaluate the spatial and temporal derivatives of the PDE. This is in contrast with conventional methods such as the finite difference method, where derivatives are only approximated with numerical difference.

Based on Equations (11) to (14), PINNs can be trained to solve PDEs iteratively like an optimization problem, which is known as the forward problem. However, when a small batch of labeled data is available, a data-based loss term can be added to the total loss of the PINN. The data-based loss is like the loss in the conventional supervised learning scheme:

$$\mathcal{L}_d = \frac{1}{N_d} \sum_{k=1}^{N_d} |\hat{u}(\mathbf{x}_d^k, t_d^k) - u(\mathbf{x}_d^k, t_d^k)|^2, \quad (15)$$

and then

$$\mathcal{L} = w_b \mathcal{L}_b + w_i \mathcal{L}_i + w_r \mathcal{L}_r + w_d \mathcal{L}_d. \quad (16)$$

The idea of adding a data-based loss has the following advantages: (1) the labeled data can serve as auxiliary data to guide the training of PINNs and thus can accelerate the training; (2) it can also be used to identify unknown parameters or discovery physics laws; (3) it enables arbitrary fusion of the experimental data into the physics-informed models. In AM processes, it is very common to use IR cameras [Hu and Kovacevic, 2003, Liu et al., 2014, Gibson et al., 2020] to monitor the melt pool temperature and geometry, where the temperature field can be partially observed. With the PINN-based hybrid thermal model, as Figure 1 illustrates, the temperature history in the entire domain can be inferred from the partially observed, sparse temperature data and the governing equation of the process.

### 3 Numerical examples

To illustrate the effectiveness of the proposed method, we first use FEM simulation results as the exact solution to benchmark the performance of the prediction results using PINN. Here, a numerical example of a bare plate scanning case is presented. The dimension of the bare plate was assumed to be 40 mm \* 10 mm \* 6 mm. A 500 W laser of 1.5 mm beam radius was used to scan the bare plate with a speed of 10 mm/s, as shown in Figure 2. The numerical example was solved using the FEM implemented in FEniCS [Alnæs et al., 2015]. A tetrahedron mesh of 0.25 mm element size was used in the simulation. The mesh consists of a total of 921,600 elements and 165,025 nodes. The Crank-Nicolson method, which is an implicit time integration scheme combining the forward and backward Euler methods [Crank and Nicolson, 1996], was used for time integration. The time step size was set as 5 ms. A total of 3 seconds of the process was simulated. The simulation parameters of this numerical example are shown in Table 1. The temperature value at each node with a frequency of 10 Hz was extracted from the simulation (4,950,750 data points in total).

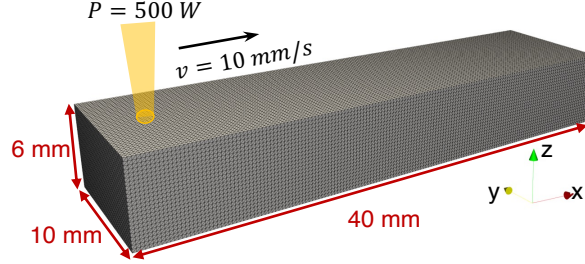


Figure 2: Schematic of the numerical example: the simulation setup.

Table 1: Simulation parameters of the numerical example.

Parameter	Value	Unit
density, $\rho$	8	$\text{g/cm}^3$
heat capacity, $C_p$	0.5	$\text{J}/(\text{g}\cdot\text{K})$
heat conductivity, $k$	10	$\text{W}/(\text{m}\cdot\text{K})$
convection coefficient, $h$	20	$\text{W}/(\text{m}^2\cdot\text{K})$
emissivity, $\varepsilon$	0.3	-
laser absorptivity, $\eta$	0.4	-
ambient temperature, $T_0$	298	K

#### 3.1 PINN trained with/without auxiliary data

As discussed in the previous section, PINN can be used as a surrogate model to solve the PDE using the PDE-based loss function defined by Equations (11) to (14). The PINN used in this example consists of 3 hidden layers with 64 neurons in each layer. The input of the PINN model is the 4-dimensional spatial-temporal coordinates, which are scaled to  $[-1, 1]$ , while the output is the temperature normalized to  $[0, 1]$ . The hyperbolic tangent function is used as the activation function for all the layers except for the output layer where the Softplus function is used to ensure a positive output, so that the predicted temperature can always be larger than the ambient temperature considering the physics of the process.

In order to form the PDE-based loss, sampling points need to be selected at the boundary, at the initial state and in the domain to calculate the residuals in Equations (12) to (14). In order to capture the highly transient boundary conditions in AM, the spatial-temporal domain was first discretized with a uniform time step of 0.05 s. At each time step, a uniform 2D grid of 1 mm interval was sampled in each surface. In particular, extra points with 0.25 mm interval were sampled in the 6 mm \* 6 mm area near the laser center, as shown in Figure 3 (a). For the residual points in the domain, it is suggested in [Lu et al., 2021a] that putting more points near the region where the gradient is large can help the training of PINN. In AM processes, it is known that the temperature gradient is large in the top layers near the laser center. Therefore, in this example we used a uniform grid of 0.5 mm within the 40 mm \* 10 mm \* 1 mm top region, which is 4 times finer than that in the lower region.

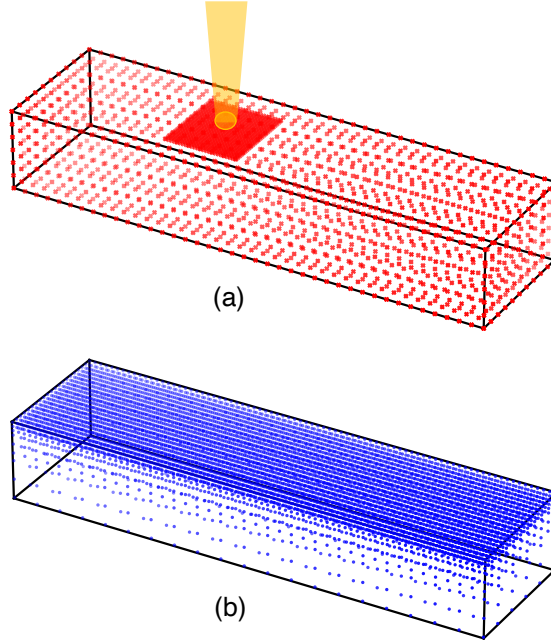


Figure 3: Sampling points at time  $t$  (a) on the boundary ; (b) in the domain.

The PINN model was implemented using PyTorch and was first trained without labeled data for 50,000 epochs using an Adam optimizer [Kingma and Ba, 2014], which took about 2.5 hours on an RTX A6000 GPU. A learning rate of  $2e-4$  was used in the training. The performance of the trained PINN model is compared with the benchmark FEM results. Figure 4 presents the comparisons between the temperature field at different time steps predicted by the PINN model and the FEM simulation from the top view and the cross-section view. It is observed that the PINN predicted temperature field matches well with the FEM results, with the RMSE of 14.07 K. The evolution of each loss term during the training process is shown in Figure 5 (a). At the beginning of the training, the PDE residual loss is small due to that Equation (1) is relatively easy to be satisfied with a uniform temperature field, while the BCs defined in Equations (4) to (7) are not satisfied at this stage. As the training proceeds, the neural network gradually learns the initial conditions and boundary conditions of the system and tends to maintain the three loss terms at the same order.

In the next step, the effect of adding the auxiliary data on the training of PINN was studied. 100,000 labeled data points were randomly selected from the benchmark FEM result as the auxiliary data to form the data loss defined in Equation (15). Two cases using the clean data and the noisy data with a Gaussian noise of standard deviation of 100 K added were tested. The entire dataset from the benchmark FEM simulation was used for validation. The same network structure and training parameters as in the case without auxiliary data were used. Figure 5 (b) is the comparison of the evolution of the normalized MSE during the PINN training without auxiliary data, with clean data, and with noisy data, respectively. It shows that the auxiliary data can accelerate the training of PINN, and eventually improve the prediction accuracy. Interestingly, the performance in the case using the noisy data is very close to that in the case using clean data, showing that PINN is robust and accepts relatively low-quality data to improve the training process. The RMSE compared with FEM results in the three cases are shown in Table 2.

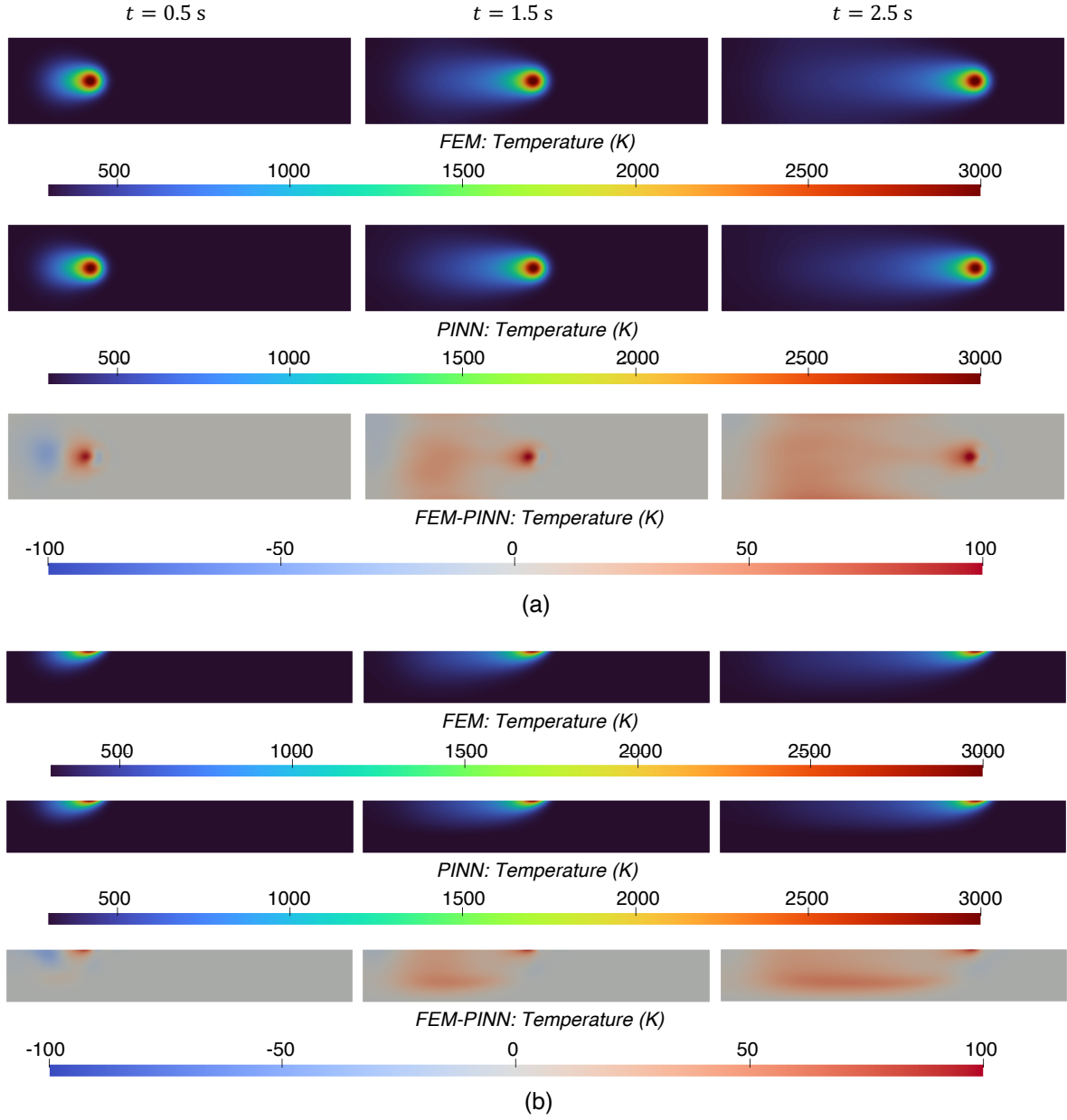


Figure 4: Comparison of the temperature field from benchmark FEM simulation and the trained PINN model: (a) Top view and (b) Cross-section view.

Table 2: Comparison of the performance of PINNs trained with and without auxiliary data.

	No auxiliary data	Clean auxiliary data	Noisy auxiliary data
RMSE (K)	14.07	3.59	3.72

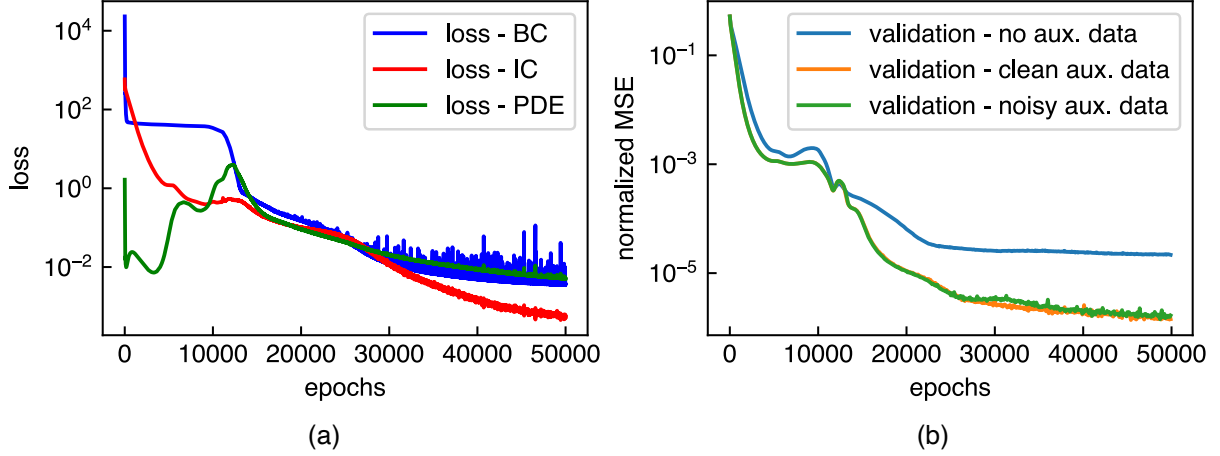


Figure 5: (a) evolution of each loss term for the PINN trained without data (2) comparison of the evolutions of the normalized MSE error of the PINN models trained with/without auxiliary data.

### 3.2 Transfer learning capabilities of PINNs

Since PINN essentially solves a non-convex optimization problem, the success of the training process is strongly affected by the initial guess of the bias and weights of the neural network. If the initial guess is close to the optimal solution, then the neural network can be trained with many fewer epochs [Bahmani and Sun, 2021]. Therefore, compared with conventional numerical methods, one advantage of using PINN to solve PDEs is that the past results can be re-utilized as a pretrained model when the parameters in the PDEs are changed.

As an example, the PINN model trained without auxiliary data discussed in the previous section is used as the pretrained model to solve an AM problem with a similar setup (see Figure 2), where the process parameter is changed from  $P = 500$  W and  $v = 10$  mm/s to  $P = 400$  W and  $v = 8$  mm/s. Figure 6 (a) shows the evolutions of each term of the loss function during the 10,000 training epochs. One can see that in this case with the pretrained model the loss function converges faster than that in Figure 5 (a). Figure 6 (b) shows the comparison of the normalized MSE during the training of the PINN started from the pretrained model and a randomly initialized model. The FEM solution of the case with  $P = 400$  W and  $v = 8$  mm/s is used as the baseline to calculate the MSE here. The PINN started from the pretrained model takes less than 1/5 of the number of epochs in the case of a randomly initialized model to reach the same accuracy, hence demonstrating the transfer learning capabilities of PINNs when solving the problem with different process parameters.

### 3.3 Data-driven discovery in AM

In AM processes, the transient thermal behavior is strongly related to not only the material properties, i.e., heat capacity, thermal conductivity, density, etc., but also the experimental conditions like laser absorptivity, convection coefficient, and ambient temperature, of which the related parameters usually need to be calibrated when the hardware setup or the environment is changed. In [Raissi et al., 2019], it is demonstrated that PINN has the ability to identify the unknown values of the parameters in PDEs by optimizing the unknown parameters and the weights and bias of the neural network at the same time:

$$\theta^*, \mu^* = \arg \min \mathcal{L}(\theta, \mu), \quad (17)$$

where  $\mu$  is the vector of unknown parameters, and  $\theta$  is the vector of weights and bias of the neural network. Here, a synthetic case is presented where the developed PINN-based thermal model can be used to identify unknown material and process parameters from partially observed sparse temperature data.

It is common to use a coaxial IR camera to monitor the melt pool temperature in PBF or DED processes to get the basic knowledge of the thermal behavior during the process and control the quality of the fabricated part. Using the partially observed temperature field data from a coaxial IR camera, the ability of PINN to identify the unknown parameters and to infer the full-field temperature data was tested. In this case, synthetic IR images were generated from the FEM simulation results described above. The temperature data was extracted in the 6 mm \* 6 mm range around the laser center with a spatial resolution of 0.25 mm and a frequency of 10 Hz. Pixels with temperatures higher than 2000 K were removed to imitate the high temperature saturation of the IR camera in the actual experiment. Gaussian noise of a



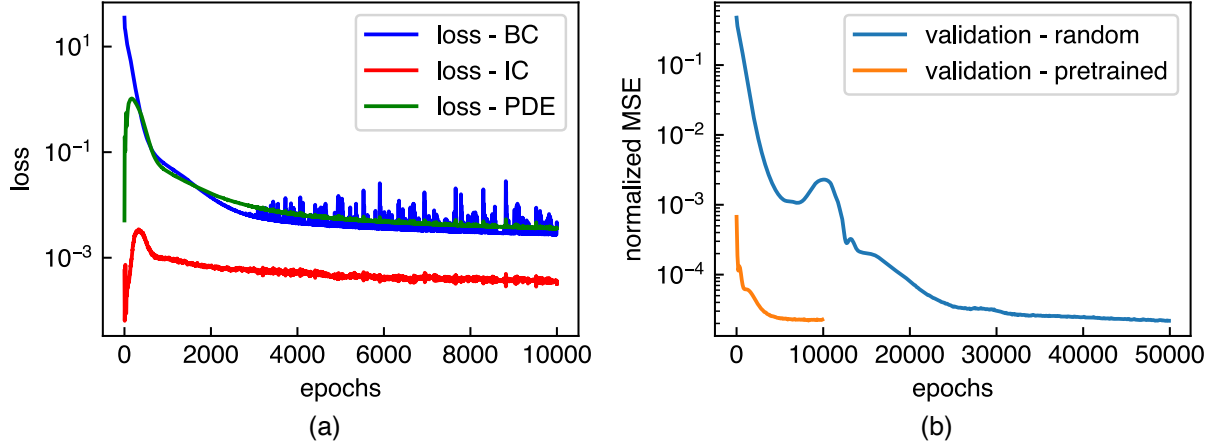


Figure 6: (a) evolution of each loss term in the case of starting from the pretrained model; (b) comparison of the evolutions of the normalized MSE error of the PINN models trained from the pretrained model and from a randomly initialized model.

standard deviation of 100 K was added to the synthetic images. Figure 7 shows the generated synthetic IR images of the melt pool.

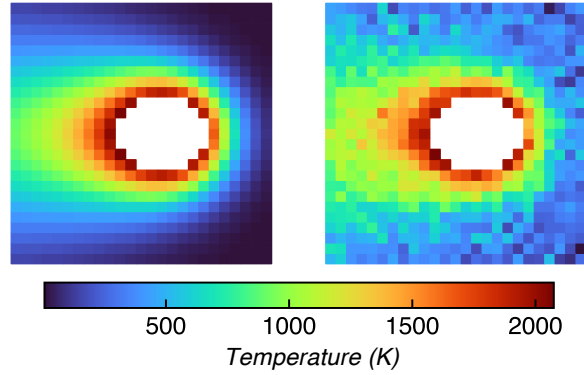


Figure 7: Generated synthetic melt pool images no noise (left) and with noise (right).

In the first example, laser absorptivity  $\eta$  was assumed to be unknown, and the PINN model was trained from randomly initialized weights and bias for 50,000 epochs. Figure 8 (a) is the evolution of each loss term while Figure 8 (b) is the history of the normalized MSE error compared to the benchmark FEM result and the value of  $\eta$  during the training process. The final identified value of  $\eta$  was 0.404, which is close to the ground truth value of 0.400. Also, the RMSE of the temperature in the full field is 11.45 K, which is comparable to the values in Table 2, showing that using PINN the full-field temperature can be well predicted from the partially observed sparse temperature data in AM processes with unknown process parameters.

In the second example, it was assumed that the material properties, i.e.,  $C_p$  and  $k$  are unknown. The evolution of each loss term and  $C_p$  and  $k$  values during the training are shown in Figure 9. Since the initial values of  $C_p$  and  $k$  were set to be small ( $1e-5$ ), the loss from the PDE residual was close to 0 at the beginning of the training and then kept increasing. After about 10,000 epochs the four loss terms reached about the same magnitude and then gradually decreased at the same time. The final identified  $C_p$  value is 0.512 J/(g·K) and  $k$  value is 9.51 W/(m·K), close to the ground truth values  $C_p = 0.500$  J/(g·K) and  $k = 10.0$  W/(m·K).

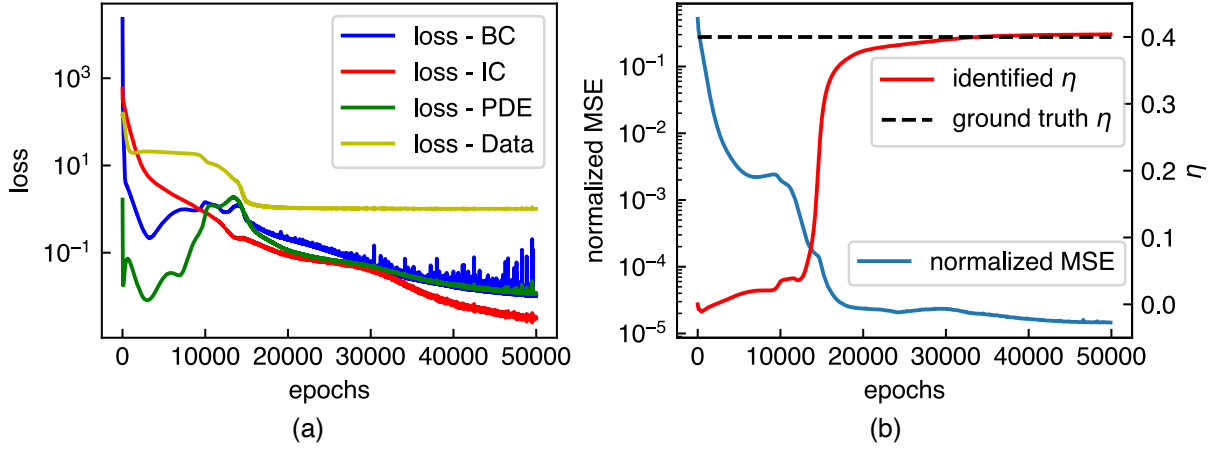


Figure 8: (a) evolution of each loss term (b) history of the normalized MSE error compared to benchmark FEM result and the value of  $\eta$  during the training process.

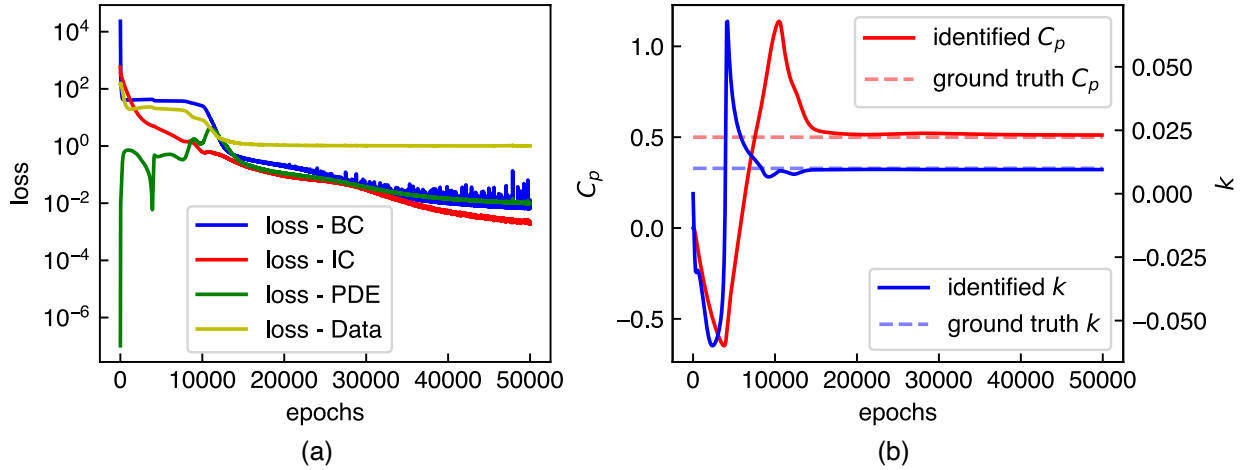


Figure 9: (a) evolution of each loss term (b) history of  $C_p$  and  $k$  values during the training process.

## 4 Experimental examples

### 4.1 Experimental setup

In this section, an experimental case is presented where the developed PINN-based thermal model of AM processes was applied to an actual DED experiment. The experiment was performed on a customized DED system, i.e., the Additive Rapid Prototyping Instrument (ARPI), developed at Northwestern University. The primary processing laser of the system is an IPG Photonics fiber laser with a 1 kW (1070 nm) maximum laser power and a 1.12 mm beam radius (measured  $1/e^2$  value). The experimental setup is shown in Figure 10. During the experiment, a FLIR A655sc IR camera with a resolution of 480 \* 640 pixels was used to capture the temperature field from the side view at a rate of 50 Hz.

In the experiment, a 40-layer thin wall part was built. Figure 11 depicts the size of the built thin wall and the substrate. The thin wall part was built using a bi-directional toolpath with a 7 mm/s scanning speed and a 500 W laser power. A 0.5 second dwell time was used between the deposition of each layer. The substrate material is AISI 1018 steel while the part material is the nickel-based alloy IN718.

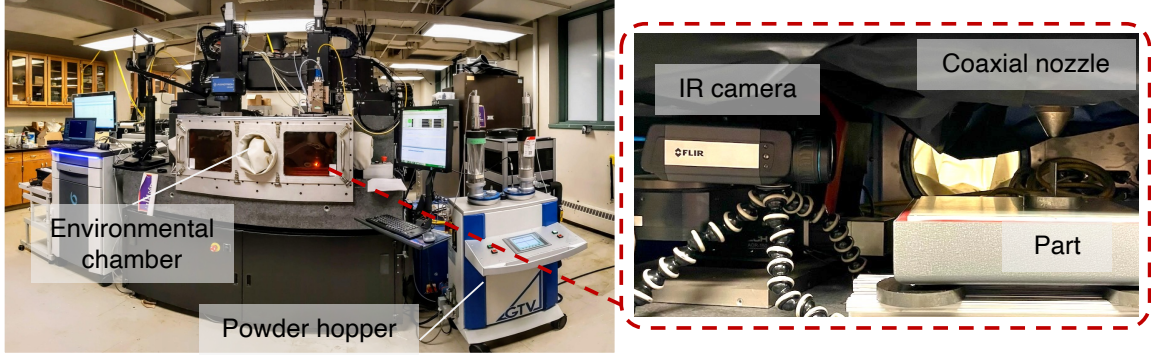


Figure 10: Experimental setup: overview of the ARPI system (left) and the temperature measurement setup (right).

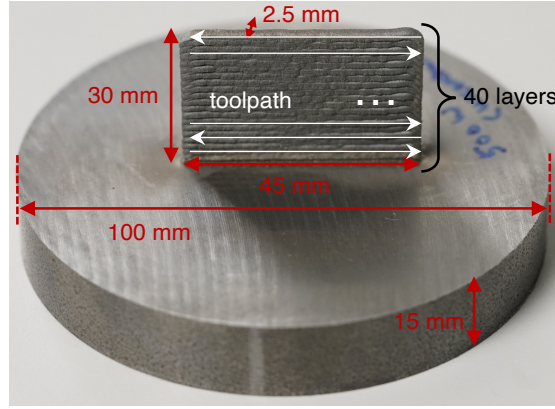


Figure 11: The built wall part from the experiment.

The FLIR IR camera was used in the experiment to measure the temperature of the side surface of the wall (about 0.2 mm spatial resolution) during the experiment. The workflow of processing the IR data is shown in Figure 12. A constant emissivity value was assumed to calculate the temperature values. The raw data was first cropped and then down-sampled to 60\*40 (0.75 mm spatial resolution) by averaging the surrounding pixels to reduce the noise of the measurement.

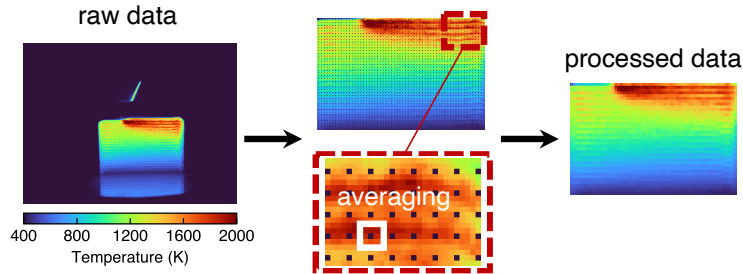


Figure 12: The workflow of processing the IR data.

## 4.2 Full field temperature prediction

In this example, the developed PINN-based hybrid model was used to infer the full temperature field from the partially observed temperature data. One basic assumption we made in this example is that the temperature is uniform along the through-the-thickness direction and the solid heat transfer through this direction can be ignored. With this assumption, the heat transfer in the thin wall case can be simplified to a 2D problem, as Figure 13 illustrates.

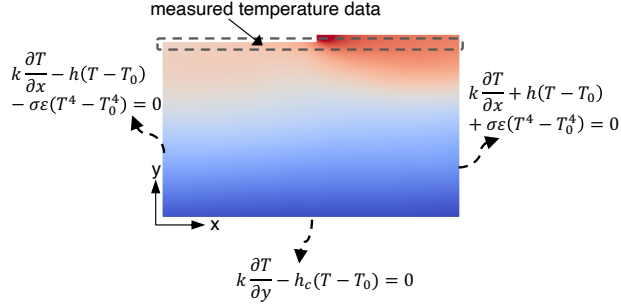


Figure 13: Illustration of the simplified 2D problem of the thin wall part with boundary conditions highlighted by equations.

The convective and radiative heat flux on the two surfaces of the wall parallel to the  $xy$  plane is treated as a heat source term. Equation (1) can be then written as:

$$\rho C_p \frac{\partial T}{\partial t} - k \nabla^2 T + \frac{2h}{w}(T - T_0) + \frac{2\sigma\epsilon}{w}(T^4 - T_0^4) = 0, \quad (18)$$

where  $w$  is the thickness of the wall, i.e., 2.5 mm in this case. The boundary condition in Equation (3) still applies to the left and right boundaries of the 2D wall. For the bottom of the wall, since the temperature of the substrate is assumed to be always equal to the ambient temperature, a flux boundary condition is assumed:

$$k \frac{\partial T}{\partial y} - h_c(T - T_0) = 0, \quad (19)$$

where  $h_c$  is equal to the ratio of the heat conductivity of the substrate material (AISI 1018: 51.9 W/(m·K)) [International et al., 1989] and the height of the substrate (15 mm). The temperature data at the last layer and the current building layer measured by the IR camera is assumed to be known and is used for calculating  $\mathcal{L}_d$  when training the PINN.

A PINN model consisting of 3 hidden layers with 64 neurons in each layer was trained for 100,000 epochs using an Adam optimizer with a learning rate of 2e-4 to solve the full-field thermal history during the deposition of the last layer from the boundary conditions described above and the measured temperature data. The parameters used in the model are given in Table 3. Temperature-dependent heat capacity and thermal conductivity values of IN718 [Mills, 2002] were used.

Table 3: Parameters used in the PINN model for the thin wall example

Parameter	Value	Unit
density, $\rho$	8.19	g/cm <sup>3</sup>
heat capacity, $C_p$	0.00020465T+0.38091	J/(g·K)
heat conductivity, $k$	0.016702T+5.5228	W/(m·K)
convection coefficient, $h$	20	W/(m <sup>2</sup> ·K)
emissivity, $\epsilon$	0.2	-
ambient temperature, $T_0$	298	K

Figure 14 depicts the results of the predicted full-field temperature from the trained PINN model compared to the measured IR data. The RMSE error between the predicted temperature field and the measured data from t=0-7 s is 47.28 K. It can be observed that the PINN model can predict the full field temperature with good accuracy. This example demonstrates the effectiveness of the proposed hybrid physics-based data-driven framework to arbitrarily fuse the experimental data into the physics-informed model for analyzing the thermal behavior in AM processes.

## 5 Conclusions and future work

In this study, a hybrid physics-based data-driven thermal model of metal AM processes based on PINNs is proposed for predicting a full-field temperature history and identifying unknown material or process parameters from partially observed temperature data. Numerical and experimental examples are provided. The fundamental findings and their corresponding impacts from the examples can be enumerated as:

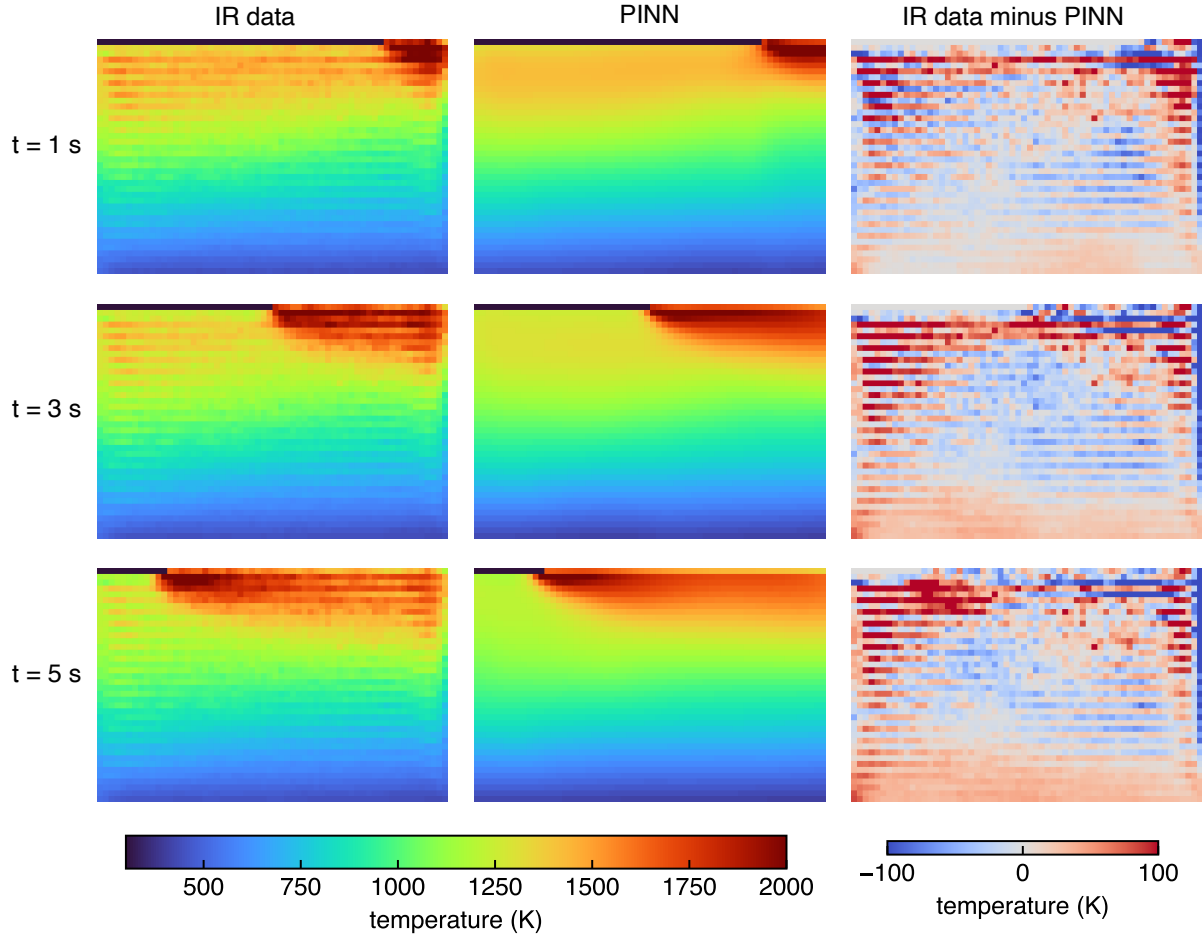


Figure 14: Results of full field temperature prediction: comparison of the measured data and prediction results.

1) PINNs can be used to solve the forward problems in AM for predicting thermal history without labeled data. In the tested numerical case, the RMSE error compared to FEM simulation results was 14.07 K. This shows that PINN can be used as an effective surrogate model for the thermal behavior in AM processes.

2) Adding auxiliary data can help the PINN model to solve forward problems with better accuracy and convergence speed. With the auxiliary data, the PINN model reached the same accuracy with only 1/3 of the number of epochs compared to that without auxiliary data. In the tested numerical case both PINNs trained with the clean data and noisy data achieved RMSE errors less than 4 K.

3) Pretraining can largely accelerate the training of PINNs. In the numerical example, the transfer learning PINN model started from a pretrained model takes less than 1/5 of the number of epochs in the case of a randomly initialized model to reach the same accuracy. Thus, the developed PINN-based thermal model is suitable in the case when multiple simulations with different materials or process parameters are desired.

4) The PINN-based hybrid thermal model can be used to identify unknown values of material and process parameters from partially observed temperature data. In the numerical example, the identified laser absorptivity, heat capacity and thermal conductivity were of less than 5% errors with the synthetic noisy IR images.

5) In the experimental example, the full-field thermal history was successfully predicted from partially observed temperature data measured by the IR camera using the developed hybrid framework. The RMSE error between the prediction and measured data was 47.28 K. It is demonstrated that the hybrid framework enables arbitrary fusion of experimental data into the PINN model, which provides a flexible way to model the thermal behavior in AM.

The current work, to the best of our knowledge, for the first time combines PINNs with experimental data for full-field temperature prediction and parameter identification in AM. In future work, more physics laws, e.g., thermal fluid and

---

vaporization, can be added to the developed hybrid framework. Since the current experimental measurements using the IR camera is not very accurate, more reliable measurement setups, e.g., the co-axial high-resolution Planck thermometry measurements [Kozjek et al., 2022], can be integrated with the PINN model. In addition to modeling the thermal behavior, the application of PINNs to model the microstructure evolution [Yang et al., 2021] and residual stress will also be developed. Moreover, since PINNs have been demonstrated to solve inverse design problems [Lu et al., 2021b] successfully, we will also explore the possibility of using PINNs to design the process parameters for AM applications.

## Code and data availability

Our code and data can be found at [https://github.com/ShuhengLiao/Physics\\_informed\\_AM](https://github.com/ShuhengLiao/Physics_informed_AM).

## Acknowledgement

This work was supported by National Institute of Standards and Technology (NIST) – Center for Hierarchical Material Design (CHiMaD) under grant No. 70 NANB19H005, and the Department of Defense Vannevar Bush Faculty Fellowship, USA N00014-19-1-2642.

## References

- Jacob Smith, Wei Xiong, Wentao Yan, Stephen Lin, Puikui Cheng, Orion L Kafka, Gregory J Wagner, Jian Cao, and Wing Kam Liu. Linking process, structure, property, and performance for metal-based additive manufacturing: computational approaches with experimental support. *Computational Mechanics*, 57(4):583–610, 2016.
- T Mukherjee, HL Wei, A De, and Tarasankar DebRoy. Heat and fluid flow in additive manufacturing—part i: Modeling of powder bed fusion. *Computational Materials Science*, 150:304–313, 2018a.
- T Mukherjee, HL Wei, A De, and Tarasankar DebRoy. Heat and fluid flow in additive manufacturing—part ii: Powder bed fusion of stainless steel, and titanium, nickel and aluminum base alloys. *Computational Materials Science*, 150: 369–380, 2018b.
- Zhengtao Gan, Hao Liu, Shaoxia Li, Xiuli He, and Gang Yu. Modeling of thermal behavior and mass transport in multi-layer laser additive manufacturing of ni-based alloy on cast iron. *International Journal of Heat and Mass Transfer*, 111:709–722, 2017.
- Zhengtao Gan, Yanping Lian, Stephen E Lin, Kevontrez K Jones, Wing Kam Liu, and Gregory J Wagner. Benchmark study of thermal behavior, surface topography, and dendritic microstructure in selective laser melting of inconel 625. *Integrating Materials and Manufacturing Innovation*, 8(2):178–193, 2019.
- Jarred C Heigel, Brandon M Lane, and Lyle E Levine. In situ measurements of melt-pool length and cooling rate during 3d builds of the metal am-bench artifacts. *Integrating Materials and Manufacturing Innovation*, 9(1):31–53, 2020.
- Ibiye Aseibichin Roberts, CJ Wang, R Esterlein, M Stanford, and DJ Mynors. A three-dimensional finite element analysis of the temperature field during laser melting of metal powders in additive layer manufacturing. *International Journal of Machine Tools and Manufacture*, 49(12-13):916–923, 2009.
- Wenyan Gao, Shusen Zhao, Yibo Wang, Zhiyan Zhang, Falan Liu, and Xuechun Lin. Numerical simulation of thermal field and fe-based coating doped ti. *International Journal of Heat and Mass Transfer*, 92:83–90, 2016.
- Erik R Denlinger and Pan Michaleris. Effect of stress relaxation on distortion in additive manufacturing process modeling. *Additive Manufacturing*, 12:51–59, 2016.
- Xufei Lu, Xin Lin, Michele Chiumenti, Miguel Cervera, Yunlong Hu, Xianglin Ji, Liang Ma, Haiou Yang, and Weidong Huang. Residual stress and distortion of rectangular and s-shaped ti-6al-4v parts by directed energy deposition: Modelling and experimental calibration. *Additive Manufacturing*, 26:166–179, 2019.
- Tianci Li, Lele Zhang, Geng Chen, Norbert Pirch, Thomas Schopphoven, Andres Gasser, and Reinhart Poprawe. A combined heat source model for the prediction of residual stress post extreme high-speed laser material deposition. *Journal of Manufacturing Processes*, 78:265–277, 2022.
- Shuheng Liao, Samantha Webster, Dean Huang, Raymonde Council, Kornel Ehmann, and Jian Cao. Simulation-guided variable laser power design for melt pool depth control in directed energy deposition. *Additive Manufacturing*, page 102912, 2022.
- Jeff E Irwin, Qian Wang, Panagiotis Pan Michaleris, Abdalla R Nassar, Yong Ren, and Christopher B Stutzman. Iterative simulation-based techniques for control of laser powder bed fusion additive manufacturing. *Additive Manufacturing*, 46:102078, 2021.

- 
- Mojtaba Mozaffar, Arindam Paul, Reda Al-Bahrani, Sarah Wolff, Alok Choudhary, Ankit Agrawal, Kornel Ehmann, and Jian Cao. Data-driven prediction of the high-dimensional thermal history in directed energy deposition processes via recurrent neural networks. *Manufacturing letters*, 18:35–39, 2018.
- Mriganka Roy and Olga Wodo. Data-driven modeling of thermal history in additive manufacturing. *Additive Manufacturing*, 32:101017, 2020.
- K Ren, Y Chew, YF Zhang, JYH Fuh, and GJ Bi. Thermal field prediction for laser scanning paths in laser aided additive manufacturing by physics-based machine learning. *Computer Methods in Applied Mechanics and Engineering*, 362: 112734, 2020.
- Zeyu Zhou, Hongyao Shen, Bing Liu, Wangzhe Du, and Jiaao Jin. Thermal field prediction for welding paths in multi-layer gas metal arc welding-based additive manufacturing: A machine learning approach. *Journal of Manufacturing Processes*, 64:960–971, 2021.
- Mojtaba Mozaffar, Shuheng Liao, Hui Lin, Kornel Ehmann, and Jian Cao. Geometry-agnostic data-driven thermal modeling of additive manufacturing processes using graph neural networks. *Additive Manufacturing*, 48:102449, 2021.
- Emmanuel Stathatos and George-Christopher Vosniakos. Real-time simulation for long paths in laser-based additive manufacturing: a machine learning approach. *The International Journal of Advanced Manufacturing Technology*, 104(5):1967–1984, 2019.
- Kari Lovise Ness, Arindam Paul, Li Sun, and Zhiliang Zhang. Towards a generic physics-based machine learning model for geometry invariant thermal history prediction in additive manufacturing. *Journal of Materials Processing Technology*, 302:117472, 2022.
- Maziar Raissi, Paris Perdikaris, and George E Karniadakis. Physics-informed neural networks: A deep learning framework for solving forward and inverse problems involving nonlinear partial differential equations. *Journal of Computational Physics*, 378:686–707, 2019.
- Maziar Raissi, Alireza Yazdani, and George Em Karniadakis. Hidden fluid mechanics: Learning velocity and pressure fields from flow visualizations. *Science*, 367(6481):1026–1030, 2020.
- Zhiping Mao, Ameya D Jagtap, and George Em Karniadakis. Physics-informed neural networks for high-speed flows. *Computer Methods in Applied Mechanics and Engineering*, 360:112789, 2020.
- Shengze Cai, Zhicheng Wang, Sifan Wang, Paris Perdikaris, and George Em Karniadakis. Physics-informed neural networks for heat transfer problems. *Journal of Heat Transfer*, 143(6), 2021.
- Ryno Laubscher. Simulation of multi-species flow and heat transfer using physics-informed neural networks. *Physics of Fluids*, 33(8):087101, 2021.
- Ehsan Haghighat, Maziar Raissi, Adrian Moure, Hector Gomez, and Ruben Juanes. A physics-informed deep learning framework for inversion and surrogate modeling in solid mechanics. *Computer Methods in Applied Mechanics and Engineering*, 379:113741, 2021.
- Enrui Zhang, Minglang Yin, and George Em Karniadakis. Physics-informed neural networks for nonhomogeneous material identification in elasticity imaging. *arXiv preprint arXiv:2009.04525*, 2020.
- Qiming Zhu, Zeliang Liu, and Jinhui Yan. Machine learning for metal additive manufacturing: Predicting temperature and melt pool fluid dynamics using physics-informed neural networks. *Computational Mechanics*, 67(2):619–635, 2021.
- Atilim Gunes Baydin, Barak A Pearlmutter, Alexey Andreyevich Radul, and Jeffrey Mark Siskind. Automatic differentiation in machine learning: a survey. *Journal of Machine Learning Research*, 18:1–43, 2018.
- Martín Abadi, Ashish Agarwal, Paul Barham, Eugene Brevdo, Zhifeng Chen, Craig Citro, Greg S Corrado, Andy Davis, Jeffrey Dean, Matthieu Devin, et al. Tensorflow: Large-scale machine learning on heterogeneous distributed systems. *arXiv preprint arXiv:1603.04467*, 2016.
- Adam Paszke, Sam Gross, Soumith Chintala, Gregory Chanan, Edward Yang, Zachary DeVito, Zeming Lin, Alban Desmaison, Luca Antiga, and Adam Lerer. Automatic differentiation in pytorch. 2017.
- Dongming Hu and Radovan Kovacevic. Sensing, modeling and control for laser-based additive manufacturing. *International Journal of Machine Tools and Manufacture*, 43(1):51–60, 2003.
- Shuang Liu, Parisa Farahmand, and Radovan Kovacevic. Optical monitoring of high power direct diode laser cladding. *Optics & Laser Technology*, 64:363–376, 2014.
- Brian T Gibson, Yashwanth Kumar Bandari, Bradley S Richardson, William C Henry, Emma J Vetland, Tayler W Sundermann, and Lonnie J Love. Melt pool size control through multiple closed-loop modalities in laser-wire directed energy deposition of ti-6al-4v. *Additive Manufacturing*, 32:100993, 2020.

- 
- Martin Alnæs, Jan Blechta, Johan Hake, August Johansson, Benjamin Kehlet, Anders Logg, Chris Richardson, Johannes Ring, Marie E Rognes, and Garth N Wells. The fenics project version 1.5. *Archive of Numerical Software*, 3(100), 2015.
- John Crank and Phyllis Nicolson. A practical method for numerical evaluation of solutions of partial differential equations of the heat-conduction type. *Advances in Computational Mathematics*, 6(1):207–226, 1996.
- Lu Lu, Xuhui Meng, Zhiping Mao, and George Em Karniadakis. Deepxde: A deep learning library for solving differential equations. *SIAM Review*, 63(1):208–228, 2021a.
- Diederik P Kingma and Jimmy Ba. Adam: A method for stochastic optimization. *arXiv preprint arXiv:1412.6980*, 2014.
- Bahador Bahmani and WaiChing Sun. Training multi-objective/multi-task collocation physics-informed neural network with student/teachers transfer learnings. *arXiv preprint arXiv:2107.11496*, 2021.
- ASM International, ASM International. Reference Publications, and American Society for Metals. Reference Publications. *ASM Engineered Materials Reference Book*. ASM International (OH), 1989.
- Kenneth C Mills. *Recommended values of thermophysical properties for selected commercial alloys*. Woodhead Publishing, 2002.
- Dominik Kozjek, Fred M Carter III, Conor Porter, Jon-Erik Mogonye, Kornel Ehmann, and Jian Cao. Data-driven prediction of next-layer melt pool temperatures in laser powder bed fusion based on co-axial high-resolution planck thermometry measurements. *Journal of Manufacturing Processes*, 79:81–90, 2022.
- Min Yang, Lu Wang, and Wentao Yan. Phase-field modeling of grain evolutions in additive manufacturing from nucleation, growth, to coarsening. *Npj Computational Materials*, 7(1):1–12, 2021.
- Lu Lu, Raphael Pestourie, Wenjie Yao, Zhicheng Wang, Francesc Verdugo, and Steven G Johnson. Physics-informed neural networks with hard constraints for inverse design. *SIAM Journal on Scientific Computing*, 43(6):B1105–B1132, 2021b.